Research Article

Interface catalytic reduction of alumina by nickle for the aluminum nanowire growth: Dynamics observed by *in situ* TEM

Zichun Wang[1,2], Dan Wang[1], Ang Li[3] (✉), Lizhuo Wang[2], Xiaodong Han[3] (✉), Yijiao Jiang[4], Jianfeng Chen[1], and Jun Huang[2] (✉)

[1] *Beijing Advanced Innovation Center for Soft Matter Science and Engineering, State Key Laboratory of Organic–Inorganic Composites, Beijing University of Chemical Technology, Beijing 100029, China*

[2] *Laboratory for Catalysis Engineering, School of Chemical and Biomolecular Engineering, The University of Sydney, New South Wales 2006, Australia*

[3] *Beijing Key Laboratory of Microstructure and Property of Advanced Materials, Beijing University of Technology, Beijing 100024, China*

[4] *Department of Engineering, Macquarie University, Sydney, New South Wales 2109, Australia*

ABSTRACT

Metal nanowires show promise in a broad range of applications and can be fabricated via a number of methods, such as vapor–liquid–solid process and template-based electrodeposition. However, the synthesis of Al nanowires (NWs) is still challenging from the stable alumina substrate. In this work, the Ni-catalyzed fabrication of Al NWs has been realized using various Al_2O_3 substrates. The growth dynamics of Al NWs on Ni/Al_2O_3 was studied using *in situ* transmission electron microscopy (TEM). The effect of alumina structures, compositions, and growth temperature were investigated. The growth of Al NWs correlates with the Na addition to the alumina support. Since no eutectic mixture of nickel aluminide was formed, a mechanism of Ni-catalyzed reduction of Al_2O_3 for Al NWs growth has been proposed instead of the vapor–liquid–solid mechanism. The key insights reported here are not restricted to Ni-catalyzed Al NWs growth but can be extended to understanding the dynamic change and catalytic performance of Ni/Al_2O_3 under working conditions.

KEYWORDS

in situ transmission electron microscopy (TEM), Al nanowires, alumina reduction, nanowire growth

1   Introduction

Extensive studies on one-dimensional (1D) metal nanowires (NWs) are motivated by their unique chemical and physical properties [1–4] and thus, find broad applications in batteries [5, 6], electronics [7–12], sensors [13–17], and catalysis [18–24]. The synthesis of metal nanowires can be achieved by the chemical vapor method and the solution processing method [25, 26]. The vapor–liquid–solid (VLS) process is a routine method for fabricating metal NWs, through gas-phase precursors dissolved into a liquid eutectic phase (called "catalyst") for supersaturation, followed by NWs growth. VLS is proposed for the anisotropic growth [27] and is directly evidenced by *in situ* transmission electron microscopy (TEM) studies [28, 29]. Direct imaging of each stage in real time provides an opportunity to detail the growth dynamics including step flow kinetics, facets at the nanowire/catalyst interface, and rearrangement of the solid catalyst surface [30]. Three steps, including seed deposition, eutectic droplet formation, and NWs growth, are directly observed by *in situ* TEM in VLS growth of Si NWs [31, 32]. A double-bilayer growth of GaN nanowires on Au seeds has been revealed by *in situ* TEM [33]. *In situ* TEM imaging of Au-catalyzed GaAs nanowire revealed that the nucleation and layer growth in VLS process can occur on similar time scales, which can be controlled independently using different growth parameters [34].

Among metal NWs, aluminum NWs are desirable for their applications in energy conversion devices (such as batteries and capacitors) [35, 36], sources for integrated circuit (IC) board or package [37], and transparent conductive/optical coatings and conductive inks [38]. So far, many different approaches have been used for the fabrication of Al nanowires, including the template-based electrodeposition or mechanical deformation techniques [39, 40], the chemical vapor deposition (CVD) method [35], the thermally-induced substitution of VLS-grown Ge NWs by Al [37], and liquid-phase replacement of Zn NWs by $AlCl_3$ [41]. Moreover, in a catalyst-free synthesis of Al NWs from Al films, the removal of surface Al_2O_3 can impede the formation of Al NWs, and thus, suggesting a key role of Al_2O_3 [42]. However, all these methods have not been adequate in the synthesis of Al NWs directly from alumina. The growing metal NWs from their cheap substrates is interesting, such as the growth of Si NWs from SiO_2 [43]. The strong oxygen affinity of Al leads to the gaseous Al precursor from H_2 reduction of alumina, which is only generated at high vacuum and temperature 1300 °C [44], and thus, Al NWs are hardly to be synthesized through the VLS mechanism as well.

In this work, we reported the fabrication of Al NWs through Ni-catalyzed reduction of Al_2O_3. The growth dynamics of the process was studied using *in situ* TEM. The growth of Al NWs strongly depends on the alumina composition/type and reduction

---

Address correspondence to Ang Li, ang.li@bjut.edu.cn; Xiaodong Han, xdhan@bjut.edu.cn; Jun Huang, jun.huang@sydney.edu.au

temperature. A mechanism has been proposed that the H spillover from Ni nanoparticle (NP) surface could promote the reduction of neighboring alumina phase and the growth of Al NWs, other than the VLS mechanism.

2   Experimental

2.1   Ni/Al$_2$O$_3$ synthesis

Ni(NO$_3$)$_3$·6H$_2$O, Al(NO$_3$)$_3$·9H$_2$O, NH$_4$OH, and Na$_2$CO$_3$·10H$_2$O were purchased from Sigma-Aldrich. The Al$_2$O$_3$ supports were prepared by a co-precipitation method as widely described elsewhere [45]. A desired amount of Al(NO$_3$)$_3$·9H$_2$O (1 M) aqueous solution was precipitated with the basic aqueous solution of NH$_4$OH (1 M) or Na$_2$CO$_3$ (1 M) at 60 °C with moderate stirring, and the pH of the suspension was kept between 7 to 9. After precipitation, the suspension was aged under agitation for an hour and then filtered under vacuum. The filter cake was rinsed with deionized water, followed by drying at 80 °C overnight. The solids were calcined with a heating rate of 1 °C·min^{-1} in static air and kept the final temperature at 800 or 1000 °C for 4 h for the synthesis of γ-Al$_2$O$_3$ or α-Al$_2$O$_3$, respectively.

Ni-loading (10 wt.%) on Al$_2$O$_3$ supports were prepared by an impregnation method. The impregnation was employed by addition of powdered Al$_2$O$_3$ to the aqueous solution of Ni(NO$_3$)$_3$·6H$_2$O (1 M). The mixture was stirred for evaporation of the mixture at 80 °C. The obtained solids were calcined in a muffle furnace at 800 °C. The samples prepared using Na$_2$CO$_3$·10H$_2$O are designated as Ni,Na/γ-Al$_2$O$_3$ and Ni,Na/α-Al$_2$O$_3$, and those prepared using NH$_4$OH are designated as Ni/γ-Al$_2$O$_3$ and Ni/α-Al$_2$O$_3$.

2.2   *In situ* environmental TEM (ETEM) studies

The videos of growth experiments were recorded on ETEM (Hitachi H-9500, 300 kV) with a H$_2$ pressure of 2 × 10^{-6} mbar. The substrate was loaded to the microscope polepiece and resistively heated to 400 °C for 1 h to reduce NiO to Ni, followed by heating to the growth temperature.

The growth mechanism was studied on an FEI Titan ETEM G2 equipped with a GIF Quantum ER, for both *ex situ* and *in situ* characterization. The Ni/Al$_2$O$_3$ nanoparticles were dispersed in ethanol by the ultrasonic method. Then a drop was cast on a PELCO TEM grid (copper grid with lacey carbon film). The gaseous environment was created inside the ETEM column with a gas flow of H$_2$ and heated by the MEMS heater integrated on the chip. Before collecting images, the sample was stabilized in the gas atmosphere for at least 5 min. The electron dose for the *in situ* TEM imaging was limited to be close to 105 e·Å^{-2}·s^{-1} in order to avoid the irradiation damage, and the image integration time was 2 s per image (0.5 fps).

3   Results and discussion

3.1   *In situ* growth of Al NWs

The Ni/Al$_2$O$_3$ catalysts were synthesized as described and confirmed by X-ray diffraction (XRD) (Fig. S1 in the Electronic Supplementary Material (ESM)), respectively. NaAlO$_2$ was clearly observed with the Na-doped samples (Ni,Na/γ-Al$_2$O$_3$ and Ni,Na/α-Al$_2$O$_3$), while no Na addition was observed with the samples prepared using NH$_4$OH. Na doping leads to the reflections of Ni/γ-Al$_2$O$_3$ and Ni/α-Al$_2$O$_3$ being slightly shifted to the higher angle. The shifting could be caused by the surface defects upon Na doping and the formation of NaAlO$_2$.

The formation of Al NWs on Ni,Na/α-Al$_2$O$_3$ has been studied

upon heating at different temperatures. Figure 1 clearly shows that the metal NWs are formed on Ni,Na/α-Al$_2$O$_3$ under heating at 400 °C in hydrogen atmosphere, with diameters ranging from 10 to 30 nm and lengths ranging from 50 to 200 nm. The Figs. 1(c1)–1(c3) display a series of time-resolved over high-resolution TEM (HRTEM) images for Al NW formation. The Al nanowire with lighter contrast was growing along with the reduction proceeding under a Ni particle. The detailed structure investigation HRTEM (Fig. 1(d)) of the nanowire tip demonstrates that the formation of metal NWs is directed with Ni heading. The Ni (111) and Ni (200) panels are observed with lattice distances of 0.21 and 0.18 nm over the top of the nanowire. In considering the reduction of Al$_2$O$_3$ in H$_2$, the NWs bodies with lattice distances of 0.24 and 0.14 nm are typically for Al (111) and Al (220), and an interface with the lattice distance of 0.28 nm was generated between Ni NPs and Al NWs. These observed panels are further confirmed on fast Fourier transform (FFT) pattern acquired on the top of Al NWs displayed on Fig. 1(e). Moreover, apart from identifying the component of the nanowire, both Ni (111) and Al (111) facets are vertical to the growth direction of Al NWs. It demonstrated the growth of Al NWs is primarily in the <111> direction under the guide of Ni particle.

The reduction of alumina with hydrogen is thermodynamically unfavored [46], even in the presence of Ni [47]. Dooley et al. [44] reported the reduction of bare alumina with atomic hydrogen to aluminium in a high-vacuum system at 750 °C and gaseous aluminium was detected at 1300 °C based on theoretical studies. Under similar vacuum conditions, the reduction of alumina to aluminium in H$_2$ could proceed at a lower temperature (400 °C) in the presence of Ni and beam irradiation here. The synthesis of Al NWs at higher heating temperatures (600 to 800 °C, Fig. S2 in the ESM) results in a significant number of dark spots. Distinct dark spots are also observed when aluminium is heated at high temperature under hydrogen atmosphere (700–1700 °C), but not under inert gases [46, 48]. The existence of these dark spots is explained by the conversion of aluminium crystal structure to a more disordered arrangement. On the other hand, the absence of Ni panel accompanied by the presence of dark spots is observed, which is similar to the formation of Si NWs catalysed by Au [7], driven by the thermomigration of metal along NWs towards the hot region. To avoid the disordered arrangement or Ni migration, further dynamic studies on the *in situ* Al NWs growth were performed at 400 °C.

3.2   Dynamics of Ni during Al NWs growth

The generation of Al NWs on Ni,Na/α-Al$_2$O$_3$, showing the best performance in the growth of Al NWs, has been studied in detail using *in situ* HRTEM. At the initial stage, the NiO NPs show a polygon shape at 0 min, and the lattice structures of NiO and α-Al$_2$O$_3$ are confirmed in the corresponding HRTEM images (Figs. 2(a) and 2(b)). The reduction of NiO to Ni resulted in polygon shape shrunk during the reaction and part of NiO was reduced to Ni (Fig. 2(c)). The lattice panel with 0.20 nm lattice distance was observed when reaction proceeded to 22 min (Fig. 2(d)) and it corresponds to the (111) panel of Ni. Compared to the *in situ* HRTEM image at 0 and 22 min, it can be determined that the size of NiO particle is reduced when exposed to H$_2$ environment. After being treated in H$_2$ for 50 min, the nickel NPs exhibit a smaller and less polygon shape (Fig. 2(f)), even after 60 min reduction (Fig. 2(g)). The reformation of NiO NPs is caused by the removal of oxygen, which is similar to that reported in the *in situ* TEM investigations on the reduction of bulk nickel oxide by Jeangros et al. [49], further confirming the reduction occurred over NiO particle. The relatively longer reduction time could be caused by the low reduction temperature used here. Notably, a slight growth of NWs was observed with the upper Ni NPs (Fig. 2(h)).
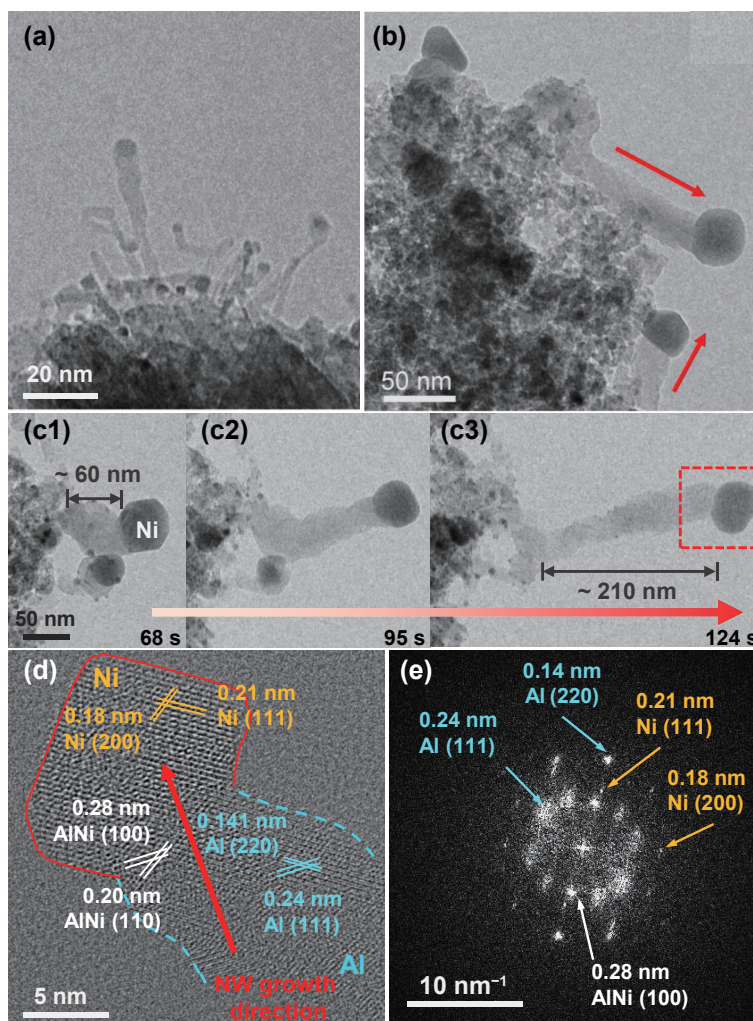
Figure 1 (a) Image of the Al NWs over Ni,Na/α-Al₂O₃. (b) Image demonstrated the Al NWs growth direction (indicated by red arrow). (c1)–(c3) Time-resolved *in situ* TEM images of Al NWs' growth over Ni,Na/α-Al₂O₃ under 2 × 10⁻⁶ mbar H₂ and heating at 400 °C. (d) *In situ* HRTEM image for the tip of the Al NWs. The red arrow indicates the Al NWs growth direction. (e) FFT pattern acquired from ROI (red square) of (d).

To gain better insight into the growth of Al NWs, *in situ* heating of Ni,Na/α-Al₂O₃ in TEM was studied at different stages (Fig. 3). The *in situ* growth of Al NWs was initially observed at 5 min 30 s (Fig. S3(b) in the ESM). The growth of two Al NWs was observed after 17 min and their length increased over 50 nm after 6 min (Figs. S3(c)–S3(e) in the ESM). Figure S3(d) in the ESM confirms the structure of Al NWs and the α-Al₂O₃ substrate by measuring the lattice distances from two different regions. Similar to the result revealed in Fig. 1, the (111) facet of Al is still vertical to the growth direction of Al NWs, double confirming the Al NWs are growing through <111> direction.

Figure 3 displays the gradual catalyst shape change at the initial stage. The reduction of NiO to Ni reduced the size of the Ni NPs. These NPs are in polygon shape with various facets (Figs. 3(b1)–3(b7)). Various phases, including Ni, Al, AlNi, and AlNi₃, are identified in the local area of Ni NPs in the corresponding FFT pattern of Fig. 3(a7). Considering the lattice distances of Al (111) (0.24 nm) and AlNi₃ (010) (0.26 nm) are similar, the Moiré pattern observed over top of Al NWs in Fig. 3(c) could be caused by superimposition of Al and AlNi₃ overlapped by an angle, which is supported by the spot pair observed in the FFT pattern. In Fig. 3, the absence of eutectic droplet formed demonstrates that the formation of Al NWs is unlikely through the VLS mechanism. The reduction temperature of 400 °C is much lower than the eutectic temperature (T_E) of aluminum nickel (> 640 °C). A vapor–solid–solid (VSS) mechanism is often proposed instead of VLS, for the growth of metal NWs with a solid catalyst [31, 50]. By

VSS, a flat interface is commonly generated, but cannot be observed here. Therefore, the mechanism for the growth of Al NWs in this work is further discussed.

3.3 Mechanism of Al NWs growth

It should be noted that the common eutectic droplet formation in the VLS growth of NWs [31, 32] is hardly to be observed during Al NWs growth by *in situ* TEM here. Mainly few layers of aluminum nickel are formed due to the reduction of Al₂O₃ at the interface of Ni and Al₂O₃. Therefore, the Ni-catalyzed Al NWs growth is proposed by reducing Al₂O₃ around Ni NPs with spillover H, other than the common VLS mechanism, as shown in Scheme 1. Ni NPs are first generated via the reduction of NiO NPs in H₂. Then the nickel mediated hydrogen spillover [51] to the Al₂O₃ support. The spillover H diffused on alumina support has been reported by van Bokhoven and co-workers [52]. Under H₂ and the beam irradiation, alumina support next to Ni NPs can be reduced to Al atoms, which diffused into the Ni NPs, forming aluminum nickel as shown in Fig. 3. The undercoordinated Ni sites in the aluminum nickel interface could increase H₂ dissociation rate and thus facilitate the reduction of alumina to Al. The Al atoms diffused and accumulated at the bottom of the nanowire as shown in Video ESM1, which promotes the Al NWs growth. It should be noted that the diffusion of spillover H depends on surface three-coordinated Al defects, showing a limitation of diffusion distance on alumina < 15 nm [52]. In this work, the diffusion and rearrangement of surface Al could
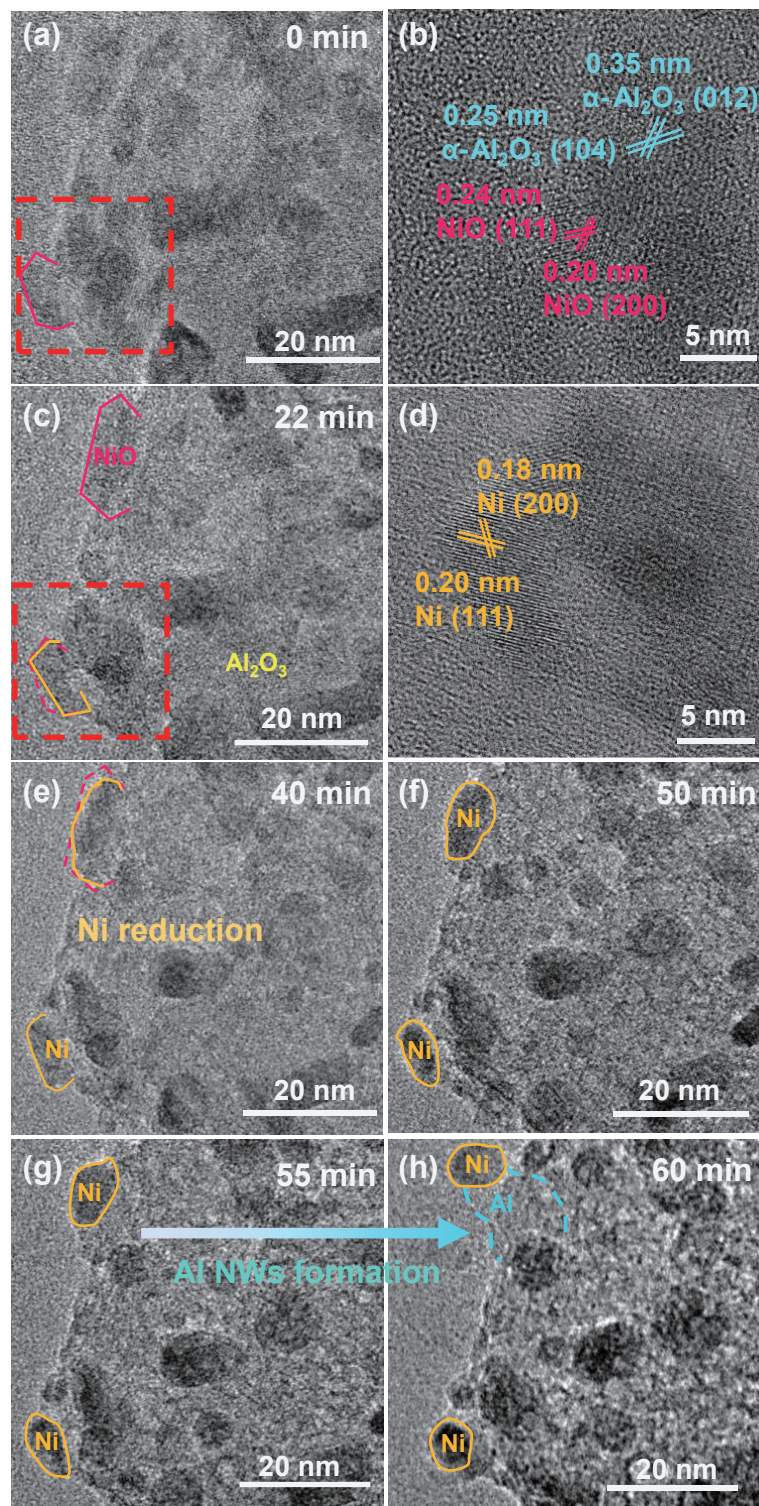
Figure 2 *In situ* TEM images recorded during reduction of Ni,Na/α-Al₂O₃ in H₂ at (a) 0, (c) 22, (e) 40, (f) 50, (g) 55, and (h) 60 min. (b) and (d) the corresponding *in situ* HRTEM images recorded at ROI (red square) of (a) and (c), respectively.

facilitate the generation of rich three-coordinated Al defects on the surface of alumina substrate and thus, promote the H spillover for the significant growth of Al NWs.

The effect of alumina structure and compositions on the formation of Al NWs are investigated using reference catalysts. As shown in Fig. S4 in the ESM, the growth of Al NWs on both the Na-doped Ni/α-Al₂O₃ and Ni/γ-Al₂O₃ catalysts (Ni,Na/α-Al₂O₃ and Ni,Na/γ-Al₂O₃) is observed. Without Na addition and the formation of AlNi phase, nearly no change of the Ni/α-Al₂O₃ and Ni/γ-Al₂O₃ catalysts prepared using NH₄OH to replace Na₂CO₃·10H₂O could be observed, even heating at 600 °C after

20 min as shown in Fig. S5 in the ESM. Compared to the Ni/α-Al₂O₃ and Ni/γ-Al₂O₃, a significant amount of NaAlO₂ is formed in those prepared using Na₂CO₃·10H₂O as shown in Fig. S1 in the ESM, which could result in surface disorders or defects on the Al₂O₃. Al₂O₃ support is generally very stable upon reduction in H₂ at 500–800 °C, even in the presence of Ni, which could not be directly used as an Al precursor for Al NWs formation [53, 54], in line with the observation of the Ni/α-Al₂O₃ and Ni/γ-Al₂O₃ catalysts prepared using NH₄OH. Therefore, the formation of NaAlO₂ is proposed to assist in the reduction of Al₂O₃. Moreover, the number and length of Al NWs formed on Ni,Na/γ-Al₂O₃ are
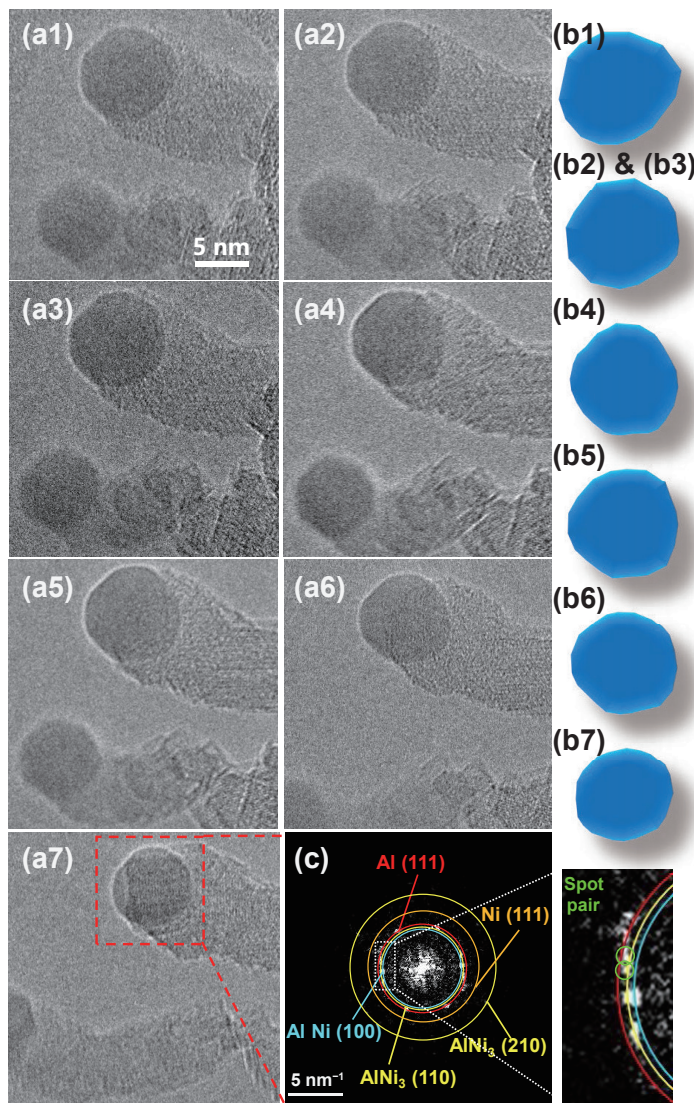
Figure 3 (a1)–(a7) TEM images recorded at the initial stages of Al NWs growth on Ni/α-Al$_2$O$_3$ in H$_2$ and (b1)–(b7) the corresponding morphology of nickel catalyst on the substrate at 400 °C. (c) The FFT pattern of ROI region (red square) of (a7).
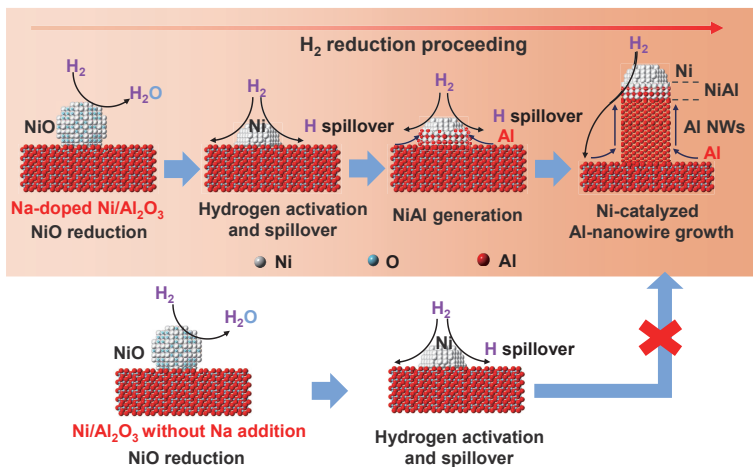
Scheme 1 Schematic diagram of the growth and *in situ* heating TEM of the Ni-catalysed Al NWs.

much less than on Ni,Na/α-Al$_2$O$_3$. The diffusion of spillover H on alumina support depends on the surface three-coordinated aluminum centers [52]. Figure S1 in the ESM shows that the Na addition could disorder the structure of α-Al$_2$O$_3$ and the content of NaAlO$_2$ is higher in the Ni,Na/α-Al$_2$O$_3$ than in the Ni,Na/γ-Al$_2$O$_3$ as indicated by the clear and large peaks. Na addition could promote the formation of surface defects, such as three-coordinated aluminum centers. Therefore, the high content of

NaAlO$_2$ in the Ni,Na/α-Al$_2$O$_3$ may promote the Ni-catalyzed reduction of alumina compared to the Ni,Na/γ-Al$_2$O$_3$.

4   Conclusions

In this work, the synthesis of Al NWs from Al$_2$O$_3$ substrates was achieved through Ni-catalysed reduction of Al$_2$O$_3$. The growth dynamics was studied using *in situ* TEM. The growth of Al NWs

is primarily in the <111> direction under the guide of Ni particle. The effect of alumina structures and compositions in Al NWs growth temperature were investigated. We find that an increasing amount of $NaAlO_2$ upon Na addition to alumina substrate can assist the Ni-catalyzed alumina reduction. The Al growth through the VLS mechanism is less favored since no eutectic mixture of nickel aluminide could be observed. Therefore, a mechanism of Ni-catalyzed reduction of Al_2O_3 for Al NWs growth has been proposed. The key insights reported here are not restricted to Ni-catalyszed Al NWs growth but can be extended to understanding the dynamic change and catalytic performance of Ni/Al_2O_3 as a popular emerging catalyst as well [45, 55–57].

Acknowledgements

Electronic Supplementary Material: Supplementary material (supporting XRD patterns, TEM images, and video) is available in the online version of this article at https://doi.org/10.1007/s12274-023-6007-1.

References

[1] Chan, C. K.; Peng, H. L.; Liu, G.; McIlwrath, K.; Zhang, X. F.; Huggins, R. A.; Cui, Y. High-performance lithium battery anodes using silicon nanowires. *Nat. Nanotechnol.* **2008**, *3*, 31–35.

[2] Hochbaum, A. I.; Chen, R. K.; Delgado, R. D.; Liang, W. J.; Garnett, E. C.; Najarian, M.; Majumdar, A.; Yang, P. D. Enhanced thermoelectric performance of rough silicon nanowires. *Nature* **2008**, *451*, 163–167.

[3] Özer, M. M.; Thompson, J. R.; Weitering, H. H. Hard superconductivity of a soft metal in the quantum regime. *Nat. Phys.* **2006**, *2*, 173–176.

[4] Zgirski, M.; Riikonen, K. P.; Touboltsev, V.; Arutyunov, K. Size dependent breakdown of superconductivity in ultranarrow nanowires. *Nano Lett.* **2005**, *5*, 1029–1033.

[5] Huang, J. Y.; Zhong, L.; Wang, C. M.; Sullivan, J. P.; Xu, W.; Zhang, L. Q.; Mao, S. X.; Hudak, N. S.; Liu, X. H.; Subramanian, A. et al. *In situ* observation of the electrochemical lithiation of a single SnO_2 nanowire electrode. *Science* **2010**, *330*, 1515–1520.

[6] Farbod, B.; Cui, K.; Kupsta, M.; Kalisvaart, W. P.; Memarzadeh, E.;

[7] Kohandehghan, A.; Zahiri, B.; Mitlin, D. Array geometry dictates electrochemical performance of Ge nanowire lithium ion battery anodes. *J. Mater. Chem. A* **2014**, *2*, 16770–16785.

[7] Kallesøe, C.; Wen, C. Y.; Booth, T. J.; Hansen, O.; Bøggild, P.; Ross, F. M.; Mølhave, K. *In situ* TEM creation and electrical characterization of nanowire devices. *Nano Lett.* **2012**, *12*, 2965–2970.

[8] Kim, J. H.; Kim, J. G.; Song, J.; Bae, T. S.; Kim, K. H.; Lee, Y. S.; Pang, Y.; Oh, K. H.; Chung, H. S. Investigation of the growth and *in situ* heating transmission electron microscopy analysis of Ag_2S-catalyzed ZnS nanowires. *Appl. Surf. Sci.* **2018**, *436*, 556–561.

[9] Cui, Y.; Wei, Q. Q.; Park, H.; Lieber, C. M. Nanowire nanosensors for highly sensitive and selective detection of biological and chemical species. *Science* **2001**, *293*, 1289–1292.

[10] Duan, X. F.; Huang, Y.; Cui, Y.; Wang, J. F.; Lieber, C. M. Indium phosphide nanowires as building blocks for nanoscale electronic and optoelectronic devices. *Nature* **2001**, *409*, 66–69.

[11] Wang, J. F.; Gudiksen, M. S.; Duan, X. F.; Cui, Y.; Lieber, C. M. Highly polarized photoluminescence and photodetection from single indium phosphide nanowires. *Science,* **2001**, *293*, 1455–1457.

[12] Senichev, A.; Corfdir, P.; Brandt, O.; Ramsteiner, M.; Breuer, S.; Schilling, J.; Geelhaar, L.; Werner, P. Electronic properties of wurtzite GaAs: A correlated structural, optical, and theoretical analysis of the same polytypic GaAs nanowire. *Nano Res.* **2018**, *11*, 4708–4721.

[13] Li, C. L.; Yamahara, H.; Lee, Y.; Tabata, H.; Delaunay, J. J. CuO nanowire/microflower/nanowire modified Cu electrode with enhanced electrochemical performance for non-enzymatic glucose sensing. *Nanotechnology* **2015**, *26*, 305503.

[14] Cho, I. H.; Kim, D. H.; Park, S. Electrochemical biosensors: Perspective on functional nanomaterials for on-site analysis. *Biomater. Res.* **2020**, *24*, 6.

[15] Yogeswaran, U.; Chen, S. M. A review on the electrochemical sensors and biosensors composed of nanowires as sensing material. *Sensors* **2008**, *8*, 290–313.

[16] Cui, Y.; Lieber, C. M. Functional nanoscale electronic devices assembled using silicon nanowire building blocks. *Science* **2001**, *291*, 851–853.

[17] He, Z.; Hassan, M.; Ju, H. X.; Wang, R.; Wang, J. L.; Chen, J. F.; Zhu, J. F.; Liu, J. W.; Yu, S. H. Stability and protection of nanowire devices in air. *Nano Res.* **2018**, *11*, 3353–3361.

[18] Steinhauer, S.; Zhao, J. L.; Singh, V.; Pavloudis, T.; Kioseoglou, J.; Nordlund, K.; Djurabekova, F.; Grammatikopoulos, P.; Sowwan, M. Thermal oxidation of size-selected Pd nanoparticles supported on CuO nanowires: The role of the CuO–Pd interface. *Chem. Mater.* **2017**, *29*, 6153–6160.

[19] Alhumaimess, M.; Lin, Z. J.; He, Q.; Lu, L.; Dimitratos, N.; Dummer, N. F.; Conte, M.; Taylor, S. H.; Bartley, J. K.; Kiely, C. J. et al. Oxidation of benzyl alcohol and carbon monoxide using gold nanoparticles supported on MnO_2 nanowire microspheres. *Chem.—Eur. J.* **2014**, *20*, 1701–1710.

[20] Christopher, P.; Linic, S. Engineering selectivity in heterogeneous catalysis: Ag nanowires as selective ethylene epoxidation catalysts. *J. Am. Chem. Soc.* **2008**, *130*, 11264–11265.

[21] Dai, D. S.; Xu, H.; Ge, L.; Han, C. C.; Gao, Y. Q.; Li, S. S.; Lu, Y. *In-situ* synthesis of CoP co-catalyst decorated $Zn_{0.5}Cd_{0.5}S$ photocatalysts with enhanced photocatalytic hydrogen production activity under visible light irradiation. *Appl. Catal. B: Environ.* **2017**, *217*, 429–436.

[22] Ma, M.; Djanashvili, K.; Smith, W. A. Controllable hydrocarbon formation from the electrochemical reduction of CO_2 over Cu nanowire arrays. *Angew. Chem., Int. Ed.* **2016**, *55*, 6680–6684.

[23] Zhang, L. C.; Wang, J. Q.; Liu, P. Y.; Liang, J.; Luo, Y. S.; Cui, G. W.; Tang, B.; Liu, Q.; Yan, X. D.; Hao, H. G. et al. $Ni(OH)_2$ nanoparticles encapsulated in conductive nanowire array for high-performance alkaline seawater oxidation. *Nano Res.* **2022**, *15*, 6084–6090.

[24] Liu, M. X.; Wu, Z. W.; Kong, X. H.; Zhang, X.; Tan, L. D.; Guo, H.; Li, C. J. One-pot synthesis of toluene from methane and methanol catalyzed by GaN nanowire. *Nano Res.* **2023**, *16*, 6512–6516.

[25] Sun, Y. G. Silver nanowires—Unique templates for functional

nanostructures. *Nanoscale* **2010**, *2*, 1626–1642.

[26] Huo, D.; Kim, M. J.; Lyu, Z. H.; Shi, Y. F.; Wiley, B. J.; Xia, Y. N. One-dimensional metal nanostructures: From colloidal syntheses to applications. *Chem. Rev.* **2019**, *119*, 8972–9073.

[27] Wagner, R. S.; Ellis, W. C. Vapor–liquid–solid mechanism of single crystal growth. *Appl. Phys. Lett.* **1964**, *4*, 89–90.

[28] Wu, J. B.; Shan, H.; Chen, W. L.; Gu, X.; Tao, P.; Song, C. Y.; Shang, W.; Deng, T. *In situ* environmental TEM in imaging gas and liquid phase chemical reactions for materials research. *Adv. Mater.* **2016**, *28*, 9686–9712.

[29] Boston, R.; Schnepp, Z.; Nemoto, Y.; Sakka, Y.; Hall, S. R. *In situ* TEM observation of a microcrucible mechanism of nanowire growth. *Science* **2014**, *344*, 623–626.

[30] Chou, Y. C.; Panciera, F.; Reuter, M. C.; Stach, E. A.; Ross, F. M. Nanowire growth kinetics in aberration corrected environmental transmission electron microscopy. *Chem. Commun.* **2016**, *52*, 5686–5689.

[31] Wen, C. Y.; Reuter, M. C.; Tersoff, J.; Stach, E. A.; Ross, F. M. Structure, growth kinetics, and ledge flow during vapor–solid–solid growth of copper-catalyzed silicon nanowires. *Nano Lett.* **2010**, *10*, 514–519.

[32] Wu, Y. Y.; Yang, P. D. Direct observation of vapor–liquid–solid nanowire growth. *J. Am. Chem. Soc.* **2001**, *123*, 3165–3166.

[33] Gamalski, A. D.; Tersoff, J.; Stach, E. A. Atomic resolution *in situ* imaging of a double-bilayer multistep growth mode in gallium nitride nanowires. *Nano Lett.* **2016**, *16*, 2283–2288.

[34] Maliakkal, C. B.; Mårtensson, E. K.; Tornberg, M. U.; Jacobsson, D.; Persson, A. R.; Johansson, J.; Wallenberg, L. R.; Dick, K. A. Independent control of nucleation and layer growth in nanowires. *ACS Nano* **2020**, *14*, 3868–3875.

[35] Benson, J.; Boukhalfa, S.; Magasinski, A.; Kvit, A.; Yushin, G. Chemical vapor deposition of aluminum nanowires on metal substrates for electrical energy storage applications. *ACS Nano* **2012**, *6*, 118–125.

[36] Sharma, S. K.; Kim, M. S.; Kim, D. Y.; Yu, J. S. Al nanorod thin films as anode electrode for Li ion rechargeable batteries. *Electrochim. Acta* **2013**, *87*, 872–879.

[37] Brunbauer, F. M.; Bertagnolli, E.; Majer, J.; Lugstein, A. Electrical transport properties of single-crystal Al nanowires. *Nanotechnology* **2016**, *27*, 385704.

[38] Lee, Y. J.; Lee, C.; Lee, H. M. Synthesis of oxide-free aluminum nanoparticles for application to conductive film. *Nanotechnology* **2018**, *29*, 055602.

[39] Kondo, T.; Kitagishi, N.; Fukushima, T.; Yanagishita, T.; Masuda, H. Fabrication of aluminum nanowires by mechanical deformation of Al using anodic porous alumina molds. *Mater. Express* **2016**, *6*, 363–366.

[40] Nesbitt, N. T.; Merlo, J. M.; Rose, A. H.; Calm, Y. M.; Kempa, K.; Burns, M. J.; Naughton, M. J. Aluminum nanowire arrays via directed assembly. *Nano Lett.* **2015**, *15*, 7294–7299.

[41] Pang, Y. T.; Meng, G. W.; Zhang, L. D.; Shan, W. J.; Zhang, C.; Gao, X. Y.; Zhao, A. W. Synthesis of ordered Al nanowire arrays. *Solid State Sci.* **2003**, *5*, 1063–1067.

[42] Lee, J. W.; Kang, M. G.; Kim, B. S.; Hong, B. H.; Whang, D.; Hwang, S. W. Single crystalline aluminum nanowires with ideal resistivity. *Scr. Mater.* **2010**, *63*, 1009–1012.

[43] Wang, N.; Tang, Y. H.; Zhang, Y. F.; Lee, C. S.; Lee, S. T. Nucleation and growth of Si nanowires from silicon oxide. *Phys. Rev. B* **1998**, *58*, R16024.

[44] Dooley, D.; Balooch, M.; Olander, D. R. Chemical reduction of refractory oxides by atomic hydrogen [Online]. https://escholarship.org/uc/item/5w0247t3 (accessed Feb 12, 2023).

[45] Wu, C. F.; Wang, Z. C.; Wang, L. Z.; Huang, J.; Williams, P. T. Catalytic steam gasification of biomass for a sustainable hydrogen future: Influence of catalyst composition. *Waste Biomass Valor* **2014**, *5*, 175–180.

[46] Braaten, O.; Kjekshus, A.; Kvande, H. The possible reduction of alumina to aluminum using hydrogen. *JOM* **2000**, *52*, 47–53.

[47] Bahari, M. B.; Phuc, N. H. H.; Alenazey, F.; Vu, K. B.; Ainirazali, N.; Vo, D. V. N. Catalytic performance of La-Ni/Al$_2$O$_3$ catalyst for CO$_2$ reforming of ethanol. *Catal. Today* **2017**, *291*, 67–75.

[48] Weller, S. W.; Montagna, A. A. Studies of alumina I. Reaction with hydrogen at elevated temperatures. *J. Catal.* **1971**, *21*, 303–311.

[49] Jeangros, Q.; Hansen, T. W.; Wagner, J. B.; Damsgaard, C. D.; Dunin-Borkowski, R. E.; Hébert, C.; Van Herle, J.; Hessler-Wyser, A. Reduction of nickel oxide particles by hydrogen studied in an environmental TEM. *J. Mater. Sci.* **2013**, *48*, 2893–2907.

[50] Jiang, Y.; Zhang, Z. F.; Yuan, W. T.; Zhang, X.; Wang, Y.; Zhang, Z. Recent advances in gas-involved *in situ* studies via transmission electron microscopy. *Nano Res.* **2018**, *11*, 42–67.

[51] Zhu, Q. Y.; Zhou, H.; Wang, L.; Wang, L.; Wang, C. T.; Wang, H.; Fang, W.; He, M. Y.; Wu, Q.; Xiao, F. S. Enhanced CO$_2$ utilization in dry reforming of methane achieved through nickel-mediated hydrogen spillover in zeolite crystals. *Nat. Catal.* **2022**, *5*, 1030–1037.

[52] Karim, W.; Spreafico, C.; Kleibert, A.; Gobrecht, J.; VandeVondele, J.; Ekinci, Y.; van Bokhoven, J. A. Catalyst support effects on hydrogen spillover. *Nature* **2017**, *541*, 68–71.

[53] Oliveira, R. L.; Bitencourt, I. G.; Passos, F. B. Partial oxidation of methane to syngas on Rh/Al$_2$O$_3$ and Rh/Ce-ZrO$_2$ catalysts. *J. Braz. Chem. Soc.* **2013**, *24*, 68–75.

[54] Le, T. A.; Kim, T. W.; Lee, S. H.; Park, E. D. CO and CO$_2$ methanation over Ni catalysts supported on alumina with different crystalline phases. *Korean J. Chem. Eng.* **2017**, *34*, 3085–3091.

[55] Wang, Y. L.; Craven, M.; Yu, X. T.; Ding, J.; Bryant, P.; Huang, J.; Tu, X. Plasma-enhanced catalytic synthesis of ammonia over a Ni/Al$_2$O$_3$ catalyst at near-room temperature: Insights into the importance of the catalyst surface on the reaction mechanism. *ACS Catal.* **2019**, *9*, 10780–10793.

[56] Foppa, L.; Margossian, T.; Kim, S. M.; Müller, C.; Copéret, C.; Larmier, K.; Comas-Vives, A. Contrasting the role of Ni/Al$_2$O$_3$ interfaces in water–gas shift and dry reforming of methane. *J. Am. Chem. Soc.* **2017**, *139*, 17128–17139.

[57] Zhu, X. L.; Huo, P. P.; Zhang, Y. P.; Cheng, D. G.; Liu, C. J. Structure and reactivity of plasma treated Ni/Al$_2$O$_3$ catalyst for CO$_2$ reforming of methane. *Appl. Catal. B: Environ.* **2008**, *81*, 132–140.